

Communications-Aware NMPC for Multi-Rotor Aerial Relay Networks Under Jamming Interference

Giuseppe Silano^{1,2}, Daniel Bonilla Licea^{3,1}, Davide Liuzza⁴, Antonio Franchi⁵, and Martin Saska¹

Abstract—Multi-Rotor Aerial Vehicles (MRAVs) are increasingly used in communication-dependent missions where connectivity loss directly compromises task execution. Existing anti-jamming strategies often decouple motion from communication, overlooking that link quality depends on vehicle attitude and antenna orientation. In coplanar platforms, “tilt-to-translate” maneuvers can inadvertently align antenna nulls with communication partners, causing severe degradation under interference. This paper presents a modular communications-aware control framework that combines a high-level max-min trajectory generator with an actuator-level Nonlinear Model Predictive Controller (NMPC). The trajectory layer optimizes the weakest link under jamming, while the NMPC enforces vehicle dynamics, actuator limits, and antenna-alignment constraints. Antenna directionality is handled geometrically, avoiding explicit radiation-pattern parametrization. The method is evaluated in a relay scenario with an active jammer and compared across coplanar and tilted-propeller architectures. Results show a near two-order-of-magnitude increase in minimum end-to-end capacity, markedly reducing outage events, with moderate average-capacity gains. Tilted platforms preserve feasibility and link quality, whereas coplanar vehicles show recurrent degradation. These findings indicate that full actuation is a key enabler of reliable communications-aware operation under adversarial directional constraints.

Index Terms—Optimization and Optimal Control, Aerial Systems: Applications, Communications-Aware Motion Planning and Control.

I. INTRODUCTION

Recent advances in sensing, communications, computation, and actuation have transformed sensor networks and robotic systems, enabling autonomous robot teams with advanced perception, interaction, and communication capabilities [1]–[4]. As a result, robotic networks are increasingly deployed in critical applications such as surveillance [5], cellular network

This work was partially supported by the CTU grant no. SGS23/177/OHK3/3T/13, the GAČR project no. 26-22419S, the EU project “Robotics and Advanced Industrial Production” (reg. no. CZ.02.01.01/00/22008/0004590), the EU project “AUTOASSESS” (grant no. 101120732), and by the research fund for the Italian Electrical System (Ricerca di Sistema) through the decree n. 388 of November 6th, 2024.

¹Department of Power Generation Technologies and Materials, Ricerca sul Sistema Energetico S.p.A., 20134 Milan, Italy.

²Faculty of Electrical Engineering, Department of Cybernetics, Czech Technical University in Prague, 12135 Prague, Czech Republic (e-mails: {giuseppe.silano, martin.saska}@fel.cvut.cz).

³College of Computing, Mohammed VI Polytechnic University, 43150 Ben Guerir, Morocco (e-mail: daniel.bonilla@um6p.ma).

⁴Department of Engineering, University of Sannio in Benevento, 82100 Benevento, Italy (e-mail: dliuzza@unisannio.it).

⁵Robotics and Mechatronics Department, Electrical Engineering, Mathematics, and Computer Science Faculty, University of Twente, 7500 AE Enschede, The Netherlands, and also with the Department of Computer, Control and Management Engineering, Sapienza University of Rome, 00185 Rome, Italy (e-mail: schol@r-franchi.eu).

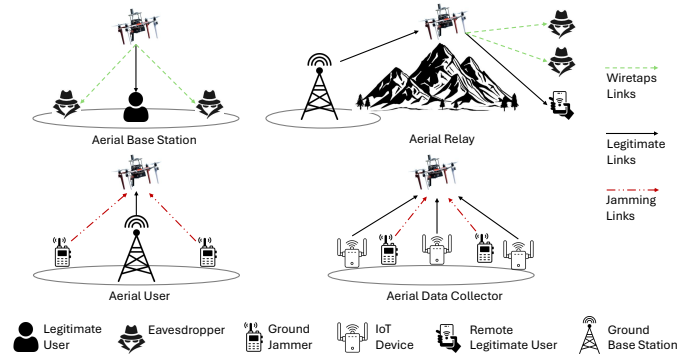


Figure 1: Illustration of adversarial threats including eavesdropping and jamming attacks.

extension [6], infrastructure monitoring [7], and data collection [8].

Radio Frequency (RF) communication is central to these networks, enabling data exchange and coordination among distributed agents. Maintaining reliable RF connectivity is challenging under mobility, which can significantly degrade links [1]–[3]. These issues become more severe in adversarial settings, where RF links are exposed to eavesdropping and jamming [9]–[11], as illustrated in Figure 1. Unmanned Aerial Vehicles (UAVs) are particularly exposed because their altitude and geometry often create Line of Sight (LoS) links with ground-based jammers [12], leaving limited shielding or rerouting options. Classical countermeasures, including frequency hopping, spectrum spreading, and transmit power control [13], provide only partial mitigation in contested environments.

UAVs are commonly divided into fixed-wing and rotary-wing platforms. *Fixed-wing* UAVs are energy-efficient for long-range missions but lack hovering capability and are unsuitable for constrained environments. *Rotary-wing* platforms, including helicopters and multi-rotors, offer vertical takeoff and landing, high maneuverability, and precise control in confined spaces at the cost of reduced endurance. Among them, multi-rotors are particularly versatile, capable of controlling position and orientation while benefiting from mechanical simplicity and redundant actuation [14]. Multi-Rotor Aerial Vehicles (MRAVs) are available in different configurations: coplanar platforms (e.g., quadrotors) provide a good balance of simplicity and control authority, whereas tilted-propeller designs offer additional actuation freedom at the expense of higher energy consumption [15], [16].

While MRAVs, like all UAVs, are inherently vulnerable to RF jamming, their agility and actuation flexibility make

them promising tools for active jamming mitigation [9], [10]. In adversarial conditions, MRAVs can adapt their position and orientation in real time to improve link quality, circumvent interference, and preserve connectivity, enabling communications-aware behaviors beyond conventional mitigation strategies [16]. Despite extensive work on trajectory design and anti-jamming techniques, most communications-aware approaches still model MRAVs as kinematic points equipped with isotropic or weakly directional radios [3], [17]. This abstraction overlooks a fundamental physical coupling: lateral motion requires body tilting, and body tilting directly reorients directional antennas. Maneuvers that are optimal from a geometric or energy perspective may therefore tend to drive the nulls of the antenna towards other communication nodes, degrading and even collapsing the communication. Ignoring this coupling yields trajectories that are dynamically feasible but communication-fragile when deployed on real platforms.

The emerging field of *communications-aware robotics* [1]–[3] addresses these challenges by embedding communication objectives into motion planning and control. By jointly optimizing mobility, connectivity, sensing, and energy, this paradigm enables robotic systems that remain effective in dynamic and adversarial environments.

This paper introduces a modular communications-aware control framework for MRAVs, composed of a *trajectory generator* and a *Nonlinear Model Predictive Controller* (NMPC). The trajectory generator computes high-level references by solving a max-min optimization problem that improves the weakest communication link under jamming. The NMPC tracks these references while enforcing actuator constraints, communication alignment, and dynamic feasibility. A key feature is that antenna directionality is incorporated through geometric alignment constraints rather than explicit antenna radiation models, capturing flight-communication coupling without requiring antenna-specific analytical parametrization. The framework applies to both coplanar and tilted-propeller MRAVs [15].

As a case study, the proposed approach is instantiated in a relay scenario in which a MRAV acts as an aerial relay between a ground base station and another mobile MRAV in the presence of an active jammer (see Figure 2). This setup is used to evaluate end-to-end communication performance and operational reliability under adversarial conditions.

II. RELATED WORK

Research on UAV-based wireless networks in adversarial environments has focused mainly on *trajectory optimization* and *anti-jamming techniques* [18]. Both aim to preserve connectivity under interference, but are usually treated separately, overlooking that MRAVs can jointly exploit mobility, attitude, and communication as a coupled resource.

A. Trajectory optimization

Trajectory optimization is a widely used approach for mitigating jamming attacks while preserving communication

connectivity. The core idea is to adapt UAV flight paths to improve link quality, reduce outages, and avoid interference. Existing methods span graph-theoretic planners, convex optimization, and Reinforcement Learning (RL). Examples include connectivity-maximizing planners [19]–[21], dynamic programming [20], and RL-based policies for reducing out-of-coverage time [21]. More advanced strategies use Deep Reinforcement Learning (DRL) to reduce mission time and outages [22], or interference-aware planning to balance energy, latency, and interference [23].

Dedicated anti-jamming trajectory design has also received significant attention. Joint trajectory–power optimization has been formulated as Stackelberg games [24], and iterative methods such as block coordinate descent and successive convex approximation have been used to construct jamming-resilient paths [20], [21]. Extensions include multiple-jammer scenarios [20], 3D planning with turning/climbing constraints [21], and UAV-to-UAV links under adversarial interference [25], [26].

Despite this progress, most trajectory-optimization frameworks embed communication metrics at the planning problem but neglect their interaction with vehicle-level dynamics and control constraints [3], [17]. As a result, communication is often optimized in isolation from the execution layer. This mismatch motivates integrated methods that jointly handle nonlinear dynamics, actuator limits, and communication objectives to ensure reliable execution in adversarial environments.

B. Anti-jamming techniques

Anti-jamming strategies can be broadly grouped into retreat strategies and physical-layer countermeasures.

Retreat strategies rely on spatial adaptation to avoid jammed regions. Classic examples include channel surfing and spatial retreating [27], [28]. For UAVs, these methods exploit mobility to evade interference with minimal hardware complexity. Game-theoretic formulations have been used to compute evasive trajectories [29], while geometric tools such as Voronoi diagrams [30] and power-based threat maps [31] provide lightweight heuristics. However, these approaches often rely on kinematic/geometric models and neglect actuator limits and aerodynamic couplings, leading to trajectories that can be dynamically infeasible or too slow for rapidly changing conditions.

Physical-layer countermeasures attempt to withstand jamming instead of evading it. Typical techniques include transmit power control to boost Signal-to-Interference-plus-Noise Ratio (SINR) [32] and error-correcting codes to mitigate packet loss [33]. More recent work uses learning-based policies, e.g. DRL, for real-time adaptive power allocation [34]. Although these approaches improve resilience, they often assume constant-power, always-on jammers, which limits applicability against adaptive adversaries. They also introduce trade-offs such as increased energy consumption or reduced throughput, both critical for resource-constrained UAV platforms.

Despite their differences, both classes largely treat motion and communication as independent. Retreat methods act on

geometry but neglect vehicle dynamics, while physical-layer methods operate at the signal level and overlook antenna orientation and motion-induced effects [35]. Consequently, neither class fully leverages actuation geometry and attitude as communication-control variables in highly dynamic environments.

Overall, existing methods either simplify vehicle dynamics or omit antenna directionality, which prevents communication objectives from being enforced at the control level. This motivates integrated frameworks that embed vehicle dynamics, actuation constraints, and communication objectives into a unified control formulation. The approach proposed here follows this direction by explicitly coupling channel alignment, jammer interference, and MRV dynamics within a single optimization architecture. To the best of the authors' knowledge, no prior work jointly enforces actuator feasibility and directional-alignment-aware communication constraints within a single receding-horizon controller.

III. CONTRIBUTIONS

This paper proposes a modular communications-aware control approach for MRVs, designed to maintain reliable connectivity in the presence of jamming interference. It combines two tightly integrated components: a trajectory generator and a communications-aware NMPC.

The *trajectory generator* computes high-level motion references (position, velocity, acceleration) by solving a max-min optimization problem that strengthens the weakest communication link under jamming. To address non-convexity, the method employs a h -norm approximation, second-order Taylor expansions, and a quadratic reformulation, enabling efficient gradient-based optimization. Bandwidth allocation is selected to balance the link capacities and maximize end-to-end throughput.

The *communications-aware NMPC* serves as the inner-loop controller, generating rotor-speed commands while enforcing actuator constraints and guaranteeing dynamic feasibility. Unlike conventional approaches, the controller jointly optimizes motion and communication objectives by embedding antenna alignment directly into the cost and constraints. A distinctive feature is its geometric treatment of antenna directionality, which avoids explicit antenna radiation pattern models and preserves alignment during agile maneuvers.

The framework is compatible with a wide range of multi-rotor designs, from coplanar to tilted-propeller platforms [15], and supports different types of antennas (as long as their radiation pattern is similar to the one shown in Figure 3). This flexibility enables deployment across platforms with varying levels of agility and actuation authority.

Specifically, this paper considers a scenario in which relay MRV-1 maintains connectivity between a ground Base Station (BS) and a mobile peer (MRV-2) in the presence of persistent, time-varying jamming, as depicted in Figure 2. This setup highlights the ability of the proposed approach to improve end-to-end communication performance while ensuring dynamically feasible motion under adversarial conditions.

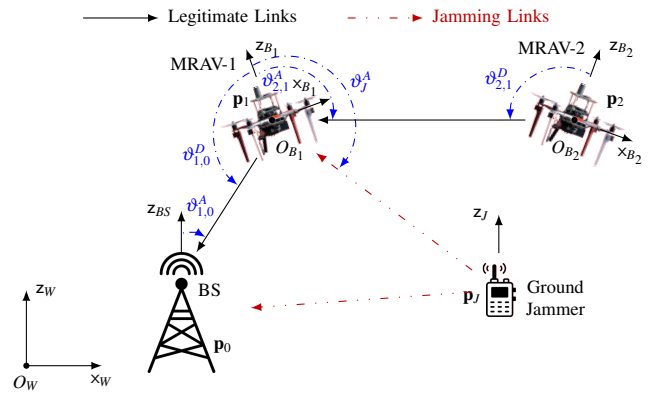


Figure 2: Schematic of MRV-1 serving as a communication relay between MRV-2 and a ground BS under jamming interference. The diagram illustrates the body reference frames $\mathcal{F}_{B_1} = \{O_{B_1}, x_{B_1}, y_{B_1}, z_{B_1}\}$ and $\mathcal{F}_{B_2} = \{O_{B_2}, x_{B_2}, y_{B_2}, z_{B_2}\}$, along with the world reference frame $\mathcal{F}_W = \{O_W, x_W, y_W, z_W\}$.

The main contributions of this paper are:

- A trajectory generator that optimizes the minimum channel capacity in a relay setting under continuous and intermittent jamming, producing dynamically feasible motion and communication references (see Section VI-A).
- A communications-aware NMPC capable of handling nonlinear vehicle dynamics, actuator limits, and antenna orientation effects without requiring explicit radiation models (see Section VI-B).
- Numerical validation in MATLAB demonstrating the framework's ability to sustain end-to-end channel capacity and generate feasible trajectories in contested environments (see Section VII).

Overall, the approach consolidates dynamics, actuation limits, and communication objectives within a unified optimization architecture, embedding antenna-alignment effects without relying on explicit radiation models and enabling connectivity-preserving maneuvers for both coplanar and tilted-propeller MRVs. Our paper is among the first to integrate a max-min communications-aware trajectory planner with a NMPC for jamming mitigation in multi-rotor communication.

IV. PROBLEM DESCRIPTION

We consider a communication relay scenario in which MRV-1 acts as an airborne relay between a mobile MRV-2 and a ground BS, while mitigating interference from a ground-based jammer (see Figure 2). The objective is to compute dynamically feasible trajectories for MRV-1 that preserve end-to-end connectivity under adversarial conditions.

The system integrates two complementary communication technologies: a RF link for high-throughput data transmission and an Optical Camera Communication (OCC) channel for inter-agent coordination. The RF link enables MRV-2 to transmit data to MRV-1, which relays it to the BS [36]. This relay configuration is required when direct MRV-2-to-BS communication is infeasible due to range limits or LoS

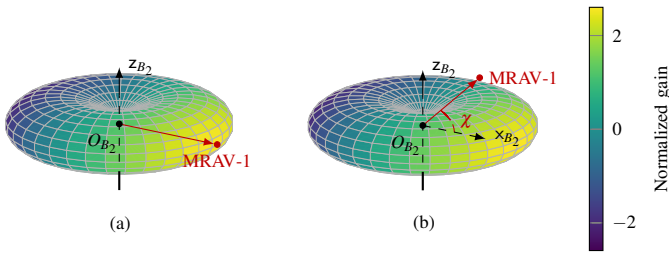


Figure 3: Normalized radiation pattern of a half-wave dipole antenna mounted along the body-frame z_B -axis. (a) MRNAV-1 aligned with the maximum-gain region in the equatorial plane. (b) MRNAV-1 tilted by an angle χ , resulting in reduced gain. Colors indicate the normalized antenna gain.

obstructions. Although the RF path provides mission-level throughput, it remains vulnerable to jamming, especially from ground-based adversaries with unobstructed LoS.

Coordination under jamming conditions is supported by an OCC system, such as the UltraViolet Direction and Ranging platform [37], [38], which provides a jamming-immune, low-latency channel for MRNAV-to-MRNAV communication. Despite its limited bit rate, OCC offers a wide field of view and is used to transmit motion intent from MRNAV-2 to MRNAV-1. This information supports predictive, coordinated NMPC on MRNAV-1. Therefore, OCC complements rather than replace RF, since it cannot provide the range or data rate required for mission communication.

Each aerial vehicle carries a single half-wave dipole antenna¹ rigidly mounted along the body z_B -axis of frame \mathcal{F}_{B_i} , with $i = \{1, 2\}$ (see Figure 2). These antennas exhibit a *doughnut-shaped* radiation pattern [17], whose inertial orientation is determined by vehicle attitude [35]. The gain function $G(\cdot)$ used in the channel model (see Section V-B) corresponds to this dipole pattern, illustrated in Figure 3. Maximum gain occurs in the equatorial plane orthogonal to z_B , while gain decays with the misalignment angle χ . Communication performance is therefore highly sensitive to attitude, especially during agile maneuvers. To isolate this coupling, we assume free-space LoS propagation without small-scale fading, a realistic approximation for high-altitude and unobstructed aerial networks [5], [7].

End-to-end communication quality is constrained by the weaker of the two RF links – from MRNAV-2 to relay or relay to BS – so overall performance is determined by the minimum SINR. Accurate modeling of antenna orientation and motion-induced misalignment is critical to maintain reliable connectivity [35].

A ground-based jammer is assumed to emit interference across the operational RF bands, thereby degrading both links simultaneously. The jammer is modeled as an isotropic radiator with uniform power distribution in all directions [5], producing persistent interference across the aerial network. Its location

¹The proposed approach does not rely on a specific parametric antenna model; it only requires a *doughnut-shaped* radiation pattern with peak broadside gain. It therefore applies to other antennas with similar directional characteristics, such as those shown in Figure 3.

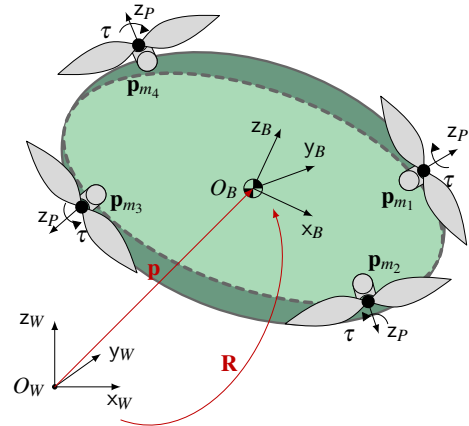


Figure 4: Schematic representation of an GTMR system with its world \mathcal{F}_W and body \mathcal{F}_B reference frames.

is initially unknown but becomes available after a short delay τ_E from jamming onset, consistent with standard localization techniques such as Received Signal Strength (RSS), Time Difference of Arrival (TDoA), or Angle of Arrival (AoA) [39], [40]. This assumption reflects adversarial scenarios involving stationary or slowly moving jammers, which can typically be localized using widely available methods.

V. PRELIMINARIES

This section introduces the models and assumptions underlying the proposed framework, covering the MRNAV dynamics, actuator constraints, and the RF communication model. Table I summarizes the notation used throughout the paper.

A. System dynamics

The MRNAV is modeled as a Generically-Tilted Multi-Rotor (GTMR) system [15], [41], actuated by N_p motor-propeller units arbitrarily placed and oriented with respect to (w.r.t) the body; the actuation layout determines whether the platform is coplanar or tilted [15], [41].

Two reference frames are used: the world frame \mathcal{F}_W and the body frame \mathcal{F}_B , whose origin is attached to the vehicle's Center of Mass (CoM), as depicted in Figure 4. The state \mathbf{x} comprises position $\mathbf{p} \in \mathbb{R}^3$ and linear velocity $\mathbf{v} = \dot{\mathbf{p}} \in \mathbb{R}^3$ (both in \mathcal{F}_W), orientation $\boldsymbol{\eta} = (\varphi, \vartheta, \psi)^\top \in \mathbb{R}^3$ (Euler angles), and angular velocity $\boldsymbol{\omega} \in \mathbb{R}^3$ (in \mathcal{F}_B).

Motor $i \in \{1, \dots, N_p\}$ delivers thrust ξ_i and torque τ_i modeled as $\xi_i = c_{\xi_i} \Omega_i z_{P_i}$ and $\tau_i = (c_{\tau_i} \mathbf{p}_{m_i} \times z_{P_i} + c_{\tau_i} z_{P_i}) \Omega_i$, where c_{ξ_i} and c_{τ_i} are thrust and torque coefficients, $\mathbf{p}_{m_i} \in \mathbb{R}^3$ is the motor position in \mathcal{F}_B , z_{P_i} its axis, and $\Omega_i \geq 0$ the (squared) motor speed [15], [41]. Collecting inputs as $\mathbf{u} = \boldsymbol{\xi} = (\xi_1, \dots, \xi_{N_p})^\top$, the Newton–Euler dynamics read:

$$\begin{cases} \dot{\mathbf{p}} = \mathbf{v} \\ \dot{\boldsymbol{\eta}} = \mathbf{T}(\boldsymbol{\eta}) \boldsymbol{\omega} \\ m \dot{\mathbf{v}} = -mg \mathbf{e}_3 + \mathbf{R}(\boldsymbol{\eta}) \mathbf{F} \mathbf{u} \\ \mathbf{J} \dot{\boldsymbol{\omega}} = -\boldsymbol{\omega} \times \mathbf{J} \boldsymbol{\omega} + \mathbf{M} \mathbf{u} \end{cases}, \quad (1)$$

where m is the mass, g the gravitational constant, $\mathbf{e}_3 = (0, 0, 1)^\top$, $\mathbf{J} \in \mathbb{R}^{3 \times 3}$ the inertia matrix in \mathcal{F}_B , $\mathbf{R}(\boldsymbol{\eta}) \in \mathbb{R}^{3 \times 3}$ the rotation from \mathcal{F}_B to \mathcal{F}_W , and $\mathbf{T}(\boldsymbol{\eta}) \in \mathbb{R}^{3 \times 3}$ the Euler-rate

Table I: Summary of notation.

Frames and Kinematics	
$\mathcal{F}_W, \mathcal{F}_{B_i}$	World and body- i frames
\mathbf{p}, \mathbf{v}	Position and linear velocity (world frame)
$\boldsymbol{\eta}, \boldsymbol{\omega}$	Orientation and angular velocity (body frame)
φ, ϑ, ψ	Roll, pitch, and yaw angles
\mathbf{R}, \mathbf{T}	Rotation and Euler rate mapping matrices
Vehicle Dynamics and Control	
$\mathbf{x}, \mathbf{u}, \bar{\mathbf{x}}$	State and input vectors, extended state vectors
m, \mathbf{J}, g, N_p	Mass, inertia, gravity, and number of propellers
c_{ξ_i}, c_{τ_i}	Thrust and torque coefficients of motor i
$\mathbf{p}_{m_i}, \mathbf{z}_{p_i}$	Position and axis of motor i
$\boldsymbol{\xi}, \boldsymbol{\tau}, \Omega_i$	Motor thrusts and torques, squared speed of motor i
\mathbf{F}, \mathbf{M}	Force/momentum allocation matrices
$\underline{\gamma}, \bar{\gamma}, \dot{\underline{\gamma}}, \dot{\bar{\gamma}}$	Bounds on propeller speed
Communication and Channel Model	
τ_E, μ	Jammer localization delay, mutual alignment threshold
$P_{U,i}, P_J, \sigma_J^2$	Tx power (node i), jammer power, and noise (node j)
$\Gamma_{i,j}$	SINR at receiver j from transmitter i
$H_{i,j}, \bar{H}_{i,j}$	Legitimate link gain and approximation ($i \rightarrow j$)
$F_{J,j}, \bar{F}_{J,j}$	Jamming link gain and upper bound (jammer $\rightarrow j$)
$G(\cdot), \bar{G}$	Antenna gain function (dipole) and maximum value
$\vartheta_{i,j}^D, \vartheta_{i,j}^A$	Departure and arrival angles ($i \rightarrow j$)
$\vartheta_{i,j}^A$	Jammer arrival angle at node j
$C_{i,j}, B_i$	Link capacity ($i \rightarrow j$) and bandwidth (Tx i)
C, \bar{C}	End-to-end capacity and approximation
$v_{i,j}$	Squared alignment measure (i, j)
$\Delta_{i,j}$	Unit vector from node ($i \rightarrow j$)
Trajectory Generation and Optimization	
N, T_s, \bullet_k	Horizon length, sampling time, and index k
\mathbf{K}, \mathbf{K}_e	Joint state vector and expansion point
$\mathbf{p}_{d,1}, \dot{\mathbf{p}}_{d,1}, \ddot{\mathbf{p}}_{d,1}$	Desired position, velocity, and acceleration of MRV-1
$\bar{f}, \hat{f}, f^{[2]}$	Inverse capacity function and approximations
δ_i	Displacement: $\mathbf{p}_i - \mathbf{p}_e$
$\mathbf{g}_1, \mathbf{H}_{ij}$	Gradient of \bar{f} w.r.t \mathbf{p}_1 and Hessian blocks
$\bar{\mathbf{x}}_{1 k}$	Extended state of MRV-1 at time k
$\mathbf{u}_{1 k}$	Control input (derivative of squared motor speeds) at k
$\mathbf{u}_{\Delta k}$	Input increment: $\mathbf{u}_{1 k} - \mathbf{u}_{1 k-1}$
\mathbf{y}_d	Reference trajectory $(\mathbf{p}_{1,d}^\top, \dot{\mathbf{p}}_{1,d}^\top, \ddot{\mathbf{p}}_{1,d}^\top)^\top$
$\boldsymbol{\rho}_{1 k}$	Thrust direction of MRV-1 in \mathcal{F}_W at k
$\boldsymbol{\rho}_{d,1 k}$	Desired (normalized) thrust direction at k of MRV-1
\mathbf{e}_k	Composite tracking error at k $(\mathbf{e}_{p k}, \mathbf{e}_{v k}, \mathbf{e}_{\rho k})^\top$
$v_{i,j k}$	Squared directional cosine from node ($i \rightarrow j$) at k
$\mathbf{e}_{\text{mis} k}$	Misalignment error vector at k
$\mathbf{Q}_e, \mathbf{Q}_u, \mathbf{Q}_v$	Stage cost weight (tracking, control, and misalignment)
$\mathbf{Q}_{e N}, \mathbf{Q}_{v N}$	Terminal cost weights
ℓ_k, ℓ_N	Stage and terminal costs
$J, q\pi$	Total cost over horizon, penalty weight for slack variable
π_k	Slack variable for alignment constraint at k

map. The allocation matrices $\mathbf{F} \in \mathbb{R}^{3 \times N_p}$ and $\mathbf{M} \in \mathbb{R}^{3 \times N_p}$ map individual motor thrusts to net force and moment at the CoM [15], [41].

To capture actuator bandwidth limits, the commanded input is defined as the time derivative of motor speeds, $\dot{\mathbf{u}} = \dot{\boldsymbol{\Omega}} \in \mathbb{R}^{N_p}$. The state is accordingly augmented as $\bar{\mathbf{x}} = (\mathbf{p}^\top, \boldsymbol{\eta}^\top, \mathbf{v}^\top, \boldsymbol{\omega}^\top, \mathbf{u}^\top)^\top \in \mathbb{R}^{12+N_p}$. This formulation enables explicit, physically meaningful actuator constraints:

$$\underline{\gamma} \leq \mathbf{u} \leq \bar{\gamma} \quad \text{and} \quad \dot{\underline{\gamma}} \leq \dot{\mathbf{u}} \leq \dot{\bar{\gamma}}, \quad (2)$$

where $\underline{\gamma}, \bar{\gamma}$ are minimum/maximum motor speeds and $\dot{\underline{\gamma}}, \dot{\bar{\gamma}}$ their acceleration bounds (possibly speed-dependent). A base-station body frame \mathcal{F}_{B_0} is also defined at \mathbf{p}_0 , aligned with \mathcal{F}_W , for notational convenience.

B. Communication channel model

As said, the RF links between MRV-1 and MRV-2 are modeled using the free-space path loss model under unobstructed LoS conditions [11]. Small-scale fading and shadowing are neglected, consistent with aerial communication scenarios where vehicles typically operate at high altitude with minimal obstacles and a dominant LoS component [5], [7]. Each MRV is equipped with a half-wave dipole antenna rigidly mounted along its body-frame z_B -axis, as illustrated in Figure 2. Consequently, the antenna's orientation in the world frame \mathcal{F}_W is directly coupled to the vehicle's attitude $\boldsymbol{\eta}$, making link performance sensitive to motion-induced misalignment.

Calling i a transmitter node and j a receiving node, the received SINR is expressed as:

$$\Gamma_{i,j} = \frac{H_{i,j}^2 P_{U,i}}{F_{J,j}^2 P_J + \sigma_J^2}, \quad (3)$$

where $P_{U,i}$ is the transmit power of the sending MRV, P_J is the jammer power, and σ_J^2 is the receiver noise at node j .

The legitimate link gain from transmitter node i to receiver node j is modeled as:

$$H_{i,j} = \frac{\sqrt{G(\vartheta_{i,j}^D) G(\vartheta_{i,j}^A)}}{\|\mathbf{p}_j - \mathbf{p}_i\|}, \quad (4)$$

where $\vartheta_{i,j}^D$ and $\vartheta_{i,j}^A$ are the departure and arrival angles of the RF link, measured w.r.t antenna boresight directions of the transmitting and receiving antennas, respectively.

Similarly, the jamming link gain from the jammer J to node j is given by:

$$F_{J,j} = \frac{\sqrt{G(\vartheta_{J,j}^A)}}{\|\mathbf{p}_J - \mathbf{p}_j\|}, \quad (5)$$

where $\vartheta_{J,j}^A$ is the AoA of the jamming signal at node j , measured relative to the orientation of the receiving antenna.

In both communication (4) and jamming (5) links, $G(\cdot)$ denotes the directional antenna gain, determined by the angular misalignment between the incident signal and the antenna boresight. The antenna gain $G(\cdot)$ is highly nonlinear w.r.t the AoA, even for simple antennas [35]. In addition, the AoA itself is highly nonlinear w.r.t the relative position and orientation of both MRVs (see Appendix A).

The link geometry is fully determined by the transmitter and receiver positions $\mathbf{p}_i, \mathbf{p}_j$, and the jammer position \mathbf{p}_J . Angle definitions and the antenna radiation model, based on the half-wave dipole pattern illustrated in Figure 3, are detailed in Appendix A. The assumption of free-space LoS propagation without small-scale fading follows the aerial communication setting discussed in Section IV.

Finally, the instantaneous capacity of the legitimate RF link from transmitter i to receiver j is computed using Shannon's formula:

$$C_{i,j} = B_i \log_2(1 + \Gamma_{i,j}), \quad (6)$$

where B_i denotes the bandwidth allocated to transmitter i , and $\Gamma_{i,j}$ is the received SINR at node j as defined in (3).

VI. MODULAR CONTROL ARCHITECTURE

To maintain reliable connectivity even under jamming attacks, this section introduces a modular control architecture for the relay MRV (MRV-1). The objective is to compute dynamically feasible trajectories that maximize end-to-end communication quality with both the source MRV (MRV-2) and the ground BS, while respecting actuator limits and accounting for motion-induced antenna misalignment which impacts the communications quality. Specifically, given the RF model in Section V-B, and assuming dynamic bandwidth allocation, the end-to-end capacity is obtained by first equalizing the capacity of both communications links, since the end-to-end rate is limited by the weaker link [42], [43]. Under this condition, each link occupies a fraction of the available bandwidth inversely proportional to its spectral efficiency, so that the total transmission time is the sum of the per-link transmission times. This leads to an equivalent end-to-end rate given by the harmonic mean [42], [43] of the individual link capacities:

$$C = \frac{B \log_2(1 + \Gamma_{2,1}) \log_2(1 + \Gamma_{1,0})}{\log_2(1 + \Gamma_{2,1}) + \log_2(1 + \Gamma_{1,0})}, \quad (7)$$

where $\Gamma_{2,1}$ and $\Gamma_{1,0}$ denote the SINR of the source-to-relay and relay-to-BS links, respectively.

Using index 0 to denote the BS and indices 1 and 2 to respectively denote MRV-1 and MRV-2, the ideal control problem is:

$$\begin{aligned} & \underset{\bar{\mathbf{x}}_1, \bar{\mathbf{u}}_1}{\text{maximize}} && C(\Gamma_{2,1}(\bar{\mathbf{x}}_1), \Gamma_{1,0}(\bar{\mathbf{x}}_1)) \\ & \text{s.t.} && \text{eq. (1),} \\ & && \underline{\gamma} \leq \mathbf{u}_1 \leq \bar{\gamma}, \quad \underline{\dot{\gamma}} \leq \dot{\mathbf{u}}_1 \leq \bar{\dot{\gamma}}, \\ & && \text{with } \Gamma_{i,j} \text{ given by (3), } (i,j) \in \{(2,1), (1,0)\}. \end{aligned} \quad (8)$$

Because $\Gamma_{i,j}$ depends nonlinearly on vehicle position and orientation through directional antenna gains (see (4) and (5)), solving (8) in real time is intractable. To enable practical use, we modify this optimization problem by adopting some conservative approximations.

In view of this, the approach proposed in this paper and presented in this section consists of two integrated modules. The first is a high-level trajectory generator, which formulates a max–min optimization problem to strengthen the weakest RF link in the presence of interference (see Section VI-A). This module incorporates time-varying channel conditions, antenna directionality, and jammer position to produce communications-aware motion references. Such references feed the second module. The latter is a low-level NMPC that tracks the references provided by the first module while enforcing vehicle dynamics and actuator constraints (see Section VI-B). Importantly, the NMPC enforces directional alignment through geometric misalignment metrics and exploits motion intent shared via OCC for coordination.

The first and second modules are described next, in Section VI-A and Section VI-B, respectively.

A. Trajectory generator

The trajectory generator produces references for MRV-1 to improve network connectivity under jamming. Its goal is to reposition the relay to maximize the end-to-end capacity between the source MRV-2 and the ground BS.

1) *Jammer and legitimate channels simplification:* To remove nonlinearities from antenna directionality, the jamming link is upper-bounded as

$$\bar{F}_{J,j} = \frac{\sqrt{\bar{G}}}{\|\mathbf{p}_J - \mathbf{p}_j\|}, \quad j \in \{1,0\}, \quad (9)$$

where $\bar{G} \triangleq \max_{\vartheta} G(\vartheta)$ is the maximum antenna gain. This represents the worst-case condition in which the jammer lies within the maximum-gain region of the MRV-1 antenna, namely, the equatorial plane of the dipole radiation pattern (see Figure 3). In this configuration, the jammer maximises the interference to the MRV-1 receiver, providing a conservative upper bound on the interference power w.r.t the MRV-1 orientation.

Similarly, the legitimate channel gain is conservatively approximated as

$$\bar{H}_{i,j} = \frac{\sqrt{\bar{\mu}} \bar{G}}{\|\mathbf{p}_j - \mathbf{p}_i\|}, \quad (i,j) \in \{(2,1), (1,0)\}. \quad (10)$$

This yields a bounded SINR $\bar{\Gamma}_{i,j}$ from (3) that captures range and alignment effects while decoupling antenna gains from the low-level NMPC optimization (see Section VI-B). The corresponding conservative end-to-end capacity is obtained by substituting $\bar{\Gamma}_{i,j}$ into the harmonic-mean formulation [42], [43] of (7):

$$\bar{C} = \frac{B \log_2(1 + \bar{\Gamma}_{2,1}) \log_2(1 + \bar{\Gamma}_{1,0})}{\log_2(1 + \bar{\Gamma}_{2,1}) + \log_2(1 + \bar{\Gamma}_{1,0})}. \quad (11)$$

2) *Quadratic cost function construction:* To obtain a cost function suitable for real-time optimization – i.e., one compatible with quadratic-programming-based NMPC solvers – we start by defining the inverse capacity function:

$$f(\boldsymbol{\kappa}, P_J) = \frac{1}{B} \left(\frac{1}{\log_2(1 + \bar{\Gamma}_{2,1})} + \frac{1}{\log_2(1 + \bar{\Gamma}_{1,0})} \right), \quad (12)$$

where $\boldsymbol{\kappa} \triangleq (\mathbf{p}_1^\top, \mathbf{p}_2^\top)^\top$ collects the relay and source positions. The source position \mathbf{p}_2 is assumed to be available through the OCC link with sufficient accuracy and update rate.

Since $f(\boldsymbol{\kappa}, P_J)$ is nonlinear and non-convex, it is locally approximated by a second-order Taylor expansion, here denoted as $f^{[2]}(\boldsymbol{\kappa}; \boldsymbol{\kappa}_e; P_J)$ (see Appendix B), around an expansion point $\boldsymbol{\kappa}_e$:

$$\begin{aligned} f^{[2]}(\boldsymbol{\kappa}; \boldsymbol{\kappa}_e, P_J) &= \bar{f}(\boldsymbol{\kappa}_e, P_J) + \nabla_{\boldsymbol{\kappa}} \bar{f}(\boldsymbol{\kappa}_e, P_J)^\top (\boldsymbol{\kappa} - \boldsymbol{\kappa}_e) + \\ &+ \frac{1}{2} (\boldsymbol{\kappa} - \boldsymbol{\kappa}_e)^\top \nabla_{\boldsymbol{\kappa}}^2 \bar{f}(\boldsymbol{\kappa}_e, P_J) (\boldsymbol{\kappa} - \boldsymbol{\kappa}_e), \end{aligned} \quad (13)$$

where \bar{f} denotes f evaluated under the conservative channel model, i.e., with the jammer gain replaced by $\bar{F}_{J,j}$ and the legitimate gain by $\bar{H}_{i,j}$. The expansion point $\boldsymbol{\kappa}_e$ is updated iteratively from previous solutions of the optimization problem, ensuring consistency across iterations. The Taylor expansion

is taken only w.r.t positions in $\boldsymbol{\kappa}$; angular dependence of $G(\cdot)$ will be instead enforced in the NMPC (see later formula (20)).

Treating the source motion as exogenous and focusing on the relay position \mathbf{p}_1 as the optimization variable, the resulting quadratic model is written as:

$$h(\mathbf{p}_1) = \mathbf{g}_1^\top \boldsymbol{\delta}_1 + \frac{1}{2} \boldsymbol{\delta}_1^\top \mathbf{H}_{11} \boldsymbol{\delta}_1 + \boldsymbol{\delta}_1^\top \mathbf{H}_{12} \boldsymbol{\delta}_2, \quad (14)$$

with $\boldsymbol{\delta}_1 = \mathbf{p}_1 - \mathbf{p}_{1_e}$ and $\boldsymbol{\delta}_2 = \mathbf{p}_2 - \mathbf{p}_{2_e}$, where \mathbf{p}_{1_e} and \mathbf{p}_{2_e} are the relay and sources positions at the expansion point. Here, \mathbf{g}_1 is the gradient of \bar{f} w.r.t \mathbf{p}_1 , and \mathbf{H}_{ij} denote the corresponding Hessian blocks (see Appendix B).

Minimizing this quadratic surrogate w.r.t to \mathbf{p}_1 yields the relay position, velocity and acceleration references:

$$\mathbf{p}_{d,1} = \mathbf{p}_{1_e} - \mathbf{H}_{11}^{-1} (\mathbf{g}_1 + \mathbf{H}_{12} \boldsymbol{\delta}_2), \quad (15)$$

$$\dot{\mathbf{p}}_{d,1} = -\mathbf{H}_{11}^{-1} \mathbf{H}_{12} \dot{\mathbf{p}}_2^\top, \quad (16)$$

$$\ddot{\mathbf{p}}_{d,1} = -\mathbf{H}_{11}^{-1} \mathbf{H}_{12} \ddot{\mathbf{p}}_2^\top. \quad (17)$$

Thus, the trajectory generator outputs position, velocity, and acceleration references consistent with channel geometry and source motion, while remaining compatible with real-time NMPC optimization (see Section VI-B).

This reformulation replaces explicit radiation-pattern models with geometric alignment constraints, yielding a tractable optimization that preserves the dominant dependence on range, antenna orientation (through $\ddot{\mathbf{p}}_{d,1}$ as it will be clear in Section VI-B), and jammer interference.

3) *Regularization for invertibility*: The computation of $\mathbf{p}_{d,1}$ requires the Hessian block \mathbf{H}_{11} (w.r.t the relay position \mathbf{p}_1) to be invertible. This condition is generally satisfied, but pathological cases – such as flat regions or saddle points of the approximated capacity function – may produce singular or ill-conditioned matrices, compromising numerical stability.

To guarantee robustness in real-time optimization, we introduce a safeguard: if \mathbf{H}_{11} is detected to be near-singular, the expansion point is perturbed slightly along the local gradient of \bar{f}

$$\boldsymbol{\kappa}'_e = \boldsymbol{\kappa}_e + \varepsilon \boldsymbol{\kappa}, \quad \|\varepsilon \boldsymbol{\kappa}\| \ll 1, \quad (18)$$

with $\varepsilon \boldsymbol{\kappa}$ chosen to restore positive definiteness and ensure invertibility. This adjustment guarantees that the quadratic approximation remains valid and the trajectory generator remains well-posed. In practice, such regularization is rarely needed, as the system evolves dynamically and successive NMPC solutions typically lie in well-conditioned regions of the cost landscape.

B. Communications-aware NMPC

This section presents the NMPC scheme used to track the reference trajectory from Section VI-A while enforcing vehicle dynamics, actuator limits, antenna alignment and communications-aware constraints. The controller operates in a receding-horizon manner, solving at each sampling instant a constrained optimization problem to generate dynamically feasible inputs consistent with both communication and actuation requirements, taking into account the communication channel in Section VI-A.

1) *Legitimate channel simplification via misalignment constraints*: To prevent degradation of the legitimate communication links due to antenna misalignments, we introduce the squared directional cosine:

$$v_{i,j} \triangleq (\langle \Delta_{i,j}, \mathbf{R}_i(\boldsymbol{\eta}_i) \mathbf{z}_{B_i} \rangle)^2, \quad (19)$$

where $\Delta_{i,j} = (\mathbf{p}_j - \mathbf{p}_i) / \|\mathbf{p}_j - \mathbf{p}_i\|$ is the unit vector from transmitter i to receiver j , $\mathbf{R}_i(\boldsymbol{\eta}_i)$ is the body-to-world rotation of node i , and \mathbf{z}_{B_i} is its body-frame boresight. The quantity $v_{i,j} \in [0, 1]$ measures angular misalignment: $v_{i,j} = 0$ when the link direction lies in the antenna's maximum gain plane (signal in the equatorial plane), and $v_{i,j} = 1$ under complete misalignment (link direction parallel to the boresight).

To ensure that the MRV-1 maintains sufficient directional alignment simultaneously toward the source and the ground BS, we impose the mutual constraint

$$(1 - v_{1,2})(1 - v_{1,0}) \geq \mu, \quad (20)$$

where $\mu \in [0, 1]$ sets the minimum joint alignment level. This condition enforces balanced antenna orientation across both legitimate links, consistent with the fact that the end-to-end performance is limited by the weakest one.

2) *Discrete-time formulation*: The system is discretized over a prediction horizon of N steps with sampling period $T_s > 0$, defining the time grid $t_k = kT_s$, $k \in \{0, \dots, N\}$. For time-indexed variables, the subscript k denotes the k th element (e.g., $\mathbf{p}_{1|k}$, $\mathbf{v}_{1|k}$). This discretization embeds the continuous-time dynamics of Section V-A into the NMPC scheme.

At prediction step k , the augmented state of MRV-1 is $\bar{\mathbf{x}}_{1|k} = (\mathbf{p}_{1|k}^\top, \boldsymbol{\eta}_{1|k}^\top, \mathbf{v}_{1|k}^\top, \boldsymbol{\omega}_{1|k}^\top, \mathbf{u}_{1|k}^\top)^\top$, and the control input is $\dot{\mathbf{u}}_{1|k}$, representing the time derivative of squared motor speeds. In our proposed architecture we consider that also MRV-2 has an onboard predictive controller and that its position, velocity and acceleration trajectories, respectively $\mathbf{p}_{2|k}$, $\dot{\mathbf{p}}_{2|k}$, and $\ddot{\mathbf{p}}_{2|k}$ for $k \in \{0, \dots, N\}$, are available to MRV-1 via OCC. This allows the trajectory generator (see Section VI-A) to provide, via the (15)-(17) evaluated at any k , the discrete time trajectory reference $\mathbf{y}_{d|k} = (\mathbf{p}_{d,1|k}^\top, \dot{\mathbf{p}}_{d,1|k}^\top, \ddot{\mathbf{p}}_{d,1|k}^\top)^\top$. This trajectory encodes the communications-aware motion plan that must be tracked at the best by the NMPC which will incorporate physical and alignment constraints.

3) *Objective function*: The NMPC objective is threefold: (i) track the communications-aware reference trajectory, (ii) enforce smooth actuator usage, and (iii) maintain antenna alignment. These objectives are encoded in stage and terminal cost terms. The composite tracking error is defined as:

$$\mathbf{e}_k = \begin{pmatrix} \mathbf{e}_{p,k} \\ \mathbf{e}_{v,k} \\ \mathbf{e}_{\rho,k} \end{pmatrix} = \begin{pmatrix} \mathbf{p}_{1|k} - \mathbf{p}_{d,1|k} \\ \mathbf{v}_{1|k} - \dot{\mathbf{p}}_{d,1|k} \\ \boldsymbol{\rho}_{1|k} - \boldsymbol{\rho}_{d,1|k} \end{pmatrix}, \quad (21)$$

where $\boldsymbol{\rho}_{1|k} = \mathbf{R}_1(\boldsymbol{\eta}_{1|k}) \mathbf{z}_{B_1}$ is the thrust direction in the world frame \mathcal{F}_W , and $\boldsymbol{\rho}_{d,1|k} = -\dot{\mathbf{p}}_{d,1|k} / \|\dot{\mathbf{p}}_{d,1|k}\|$ is the desired unit thrust direction. This error penalizes deviations in position, velocity, and orientation, ensuring coordinated tracking of dy-

namically feasible paths. To discourage aggressive actuation, the variation in control input is penalized:

$$\dot{\mathbf{u}}_{\Delta|k} = \dot{\mathbf{u}}_{1|k} - \dot{\mathbf{u}}_{1|k-1}, \quad (22)$$

where $\dot{\mathbf{u}}_{1|k-1}$ denotes the control input at the previous prediction step, and for $k=0$ it is initialized with the last control action applied to the system. This penalization promotes smooth control inputs and respects actuator bandwidth. To account for communication quality, we penalize antenna misalignment. For the two active links (source-to-relay and relay-to-BS), we define the misalignment penalty vector as:

$$\mathbf{e}_{\text{mis}|k} = \begin{pmatrix} v_{1,2|k} \\ v_{1,0|k} \end{pmatrix}, \quad (23)$$

which collects the penalties for both links. Since $v_{i,j} \in [0, 1]$ increases with antenna misalignment, this vector directly penalizes directional degradation on the source-to-relay and relay-to-BS links. The complete stage cost at time step k is then defined as:

$$\ell_k = \mathbf{e}_k^\top \mathbf{Q}_e \mathbf{e}_k + \dot{\mathbf{u}}_{\Delta|k}^\top \mathbf{Q}_u \dot{\mathbf{u}}_{\Delta|k} + \mathbf{e}_{\text{mis}|k}^\top \mathbf{Q}_v \mathbf{e}_{\text{mis}|k}, \quad (24)$$

where $\mathbf{Q}_e \succeq 0$, $\mathbf{Q}_u \succ 0$, and $\mathbf{Q}_v \succeq 0$ are design matrices tuning the trade-off between tracking fidelity, control smoothness, and antenna alignment. At the terminal step N , we impose a final cost to ensure long-horizon consistency:

$$\ell_N = \mathbf{e}_N^\top \mathbf{Q}_{e|N} \mathbf{e}_N + \mathbf{e}_{\text{mis}|N}^\top \mathbf{Q}_{v|N} \mathbf{e}_{\text{mis}|N}, \quad (25)$$

with $\mathbf{Q}_{e|N} \succeq 0$ and $\mathbf{Q}_{v|N} \succeq 0$ denoting terminal cost weights.

The total cost minimized over the prediction horizon is:

$$J = \sum_{k=0}^{N-1} \ell_k + \ell_N. \quad (26)$$

This cost explicitly couples vehicle dynamics and RF link quality, ensuring dynamically feasible tracking that preserves communication reliability.

4) *Optimal control problem:* The communications-aware NMPC is posed as a finite-horizon optimization problem:

$$\underset{\bar{\mathbf{x}}_1, \dot{\mathbf{u}}_1, \pi_k}{\text{minimize}} \quad \sum_{k=0}^{N-1} \ell_k + \ell_N + \sum_{k=0}^N q_\pi \pi_k^2 \quad (27a)$$

$$\text{s.t.} \quad \bar{\mathbf{x}}_{1,0} = \bar{\mathbf{x}}_{1|k}, \quad (27b)$$

$$\bar{\mathbf{x}}_{1|k+1} = \Phi(\bar{\mathbf{x}}_{1|k}, \dot{\mathbf{u}}_{1|k}), \quad k = \{0, \dots, N-1\}, \quad (27c)$$

$$\underline{\gamma} \leq \mathbf{u}_{1|k} \leq \bar{\gamma}, \quad k = \{0, \dots, N-1\}, \quad (27d)$$

$$\underline{\dot{\gamma}} \leq \dot{\mathbf{u}}_{1|k} \leq \dot{\bar{\gamma}}, \quad k = \{0, \dots, N-1\}, \quad (27e)$$

$$(1 - v_{1,2|k})(1 - v_{1,0|k}) \geq \mu - \pi_k, \quad (27f)$$

$$\pi_k \geq 0, \quad k = \{0, \dots, N\}. \quad (27g)$$

Problem (27) minimizes the cost function (27a), which combines the stage (ℓ_k) and terminal (ℓ_N) costs, with a quadratic penalty on the slack variable π_k , scaled by $q_\pi \in \mathbb{R}_{>0}$. The slack variable preserves feasibility when alignment constraints cannot be strictly satisfied, while the penalty discourages excessive violations. The cost balances three objectives: reference tracking (weighted by \mathbf{Q}_e and $\mathbf{Q}_{e|N}$), smooth actuation via penalization of rotor acceleration variations (weighted by

\mathbf{Q}_u), and communication quality through alignment indicators (weighted by \mathbf{Q}_v and $\mathbf{Q}_{v|N}$). The product form of the alignment constraint (27f) prevents over-constraining the problem by allowing compensation between links.

The system evolves according to the augmented discretized dynamics introduced in Section V-A, where motor accelerations act as control inputs. The initial state is enforced through (27b), while the discrete-time state-transition map $\Phi(\cdot)$ in (27c) corresponds to the numerical integration of the continuous-time multi-rotor model (1) over a single sampling interval. Actuator feasibility is guaranteed by constraints (27d) and (27e), which impose saturation limits and rate bounds on the propeller velocities, ensuring that all computed control actions remain physically realizable.

Communication requirements are enforced through the alignment constraint (27f), which builds on the mutual misalignment condition introduced in (20). The constraint uses the squared directional cosines $v_{1,2|k}$ and $v_{1,0|k}$ to quantify antenna alignment at each end of the link, and their product ensures that sufficient gain is preserved jointly across both hops. The threshold $\mu \in [0, 1]$ specifies the minimum acceptable alignment level, thereby embedding directional communication requirements directly into the NMPC formulation. To preserve feasibility under adverse conditions, the slack variable π_k in (27g) allows controlled relaxation of the alignment requirement. Importantly, the use of a single mutual constraint (27f) – rather than separate bounds on each link – prevents over-constraining the optimization and enables the controller to allocate alignment effort adaptively between the two links in a coordinated and computationally efficient manner.

Overall, the proposed formulation integrates vehicle dynamics, actuator limits, and communications-awareness into a unified predictive optimization framework, enabling the relay MRV to maintain robust operation under real-world communication and control constraints.

VII. SIMULATION RESULTS

To assess the proposed modular communications-aware control framework, numerical simulations were conducted in MATLAB using the MATMPC toolbox [44]. The nonlinear optimal control problem was discretized via a fourth-order Runge–Kutta scheme with a fixed sampling period of $T_s = 15$ ms and solved using the qpOASES quadratic programming solver [45]. All simulations were executed on a workstation equipped with an Intel® Core™ i7-8565U CPU (1.80 GHz) and 32 GB RAM running Ubuntu 20.04.

The simulation emulates a power-line inspection mission. The source vehicle (MRV-2) follows a predefined inspection trajectory adapted from [46], which brings it first to the mid-height of the tower structure and subsequently to the insulator region near the top (approximately 18 m in height and 3 m in width). This motion reflects typical inspection waypoints and induces significant variation in LoS geometry. The relay (MRV-1) continuously repositions itself to maintain directional alignment with both MRV-2 and the ground BS, counteracting interference from a stationary RF jammer

Table II: Optimization parameters.

Sym.	Value	Sym.	Value
\mathbf{p}_0	$[0, 0, 0]^T$ m	$\boldsymbol{\eta}_0, \boldsymbol{\eta}_{1 0}, \boldsymbol{\eta}_{2 0}$	$[0, 0, 0]^T$ rad
$\mathbf{p}_{1 0}$	$[-6.95, 5.79, 1.72]^T$ m	D, \bar{G}	1.64, 1
$\mathbf{p}_{2 0}$	$[-3.04, 5.79, 1.72]^T$ m	μ, B	0.2, 1
\mathbf{p}_J	$[-6.95, -5.79, 1.72]^T$ m	$\boldsymbol{\eta}_J$	$[0, 0, 0]^T$ rad
c_s^x, c_τ	$1.18 \times 10^{-3}, 2.5 \times 10^{-5}$	\mathbf{J}	$\text{diag}(0.11, 0.11, 0.19)$ kgm ²
T_s, N	15ms, 50	g, m, N_p	$9.81 \text{ ms}^{-2}, 2.57 \text{ kg}, 6$
$\tilde{\gamma}, \tilde{\gamma}$	100, 16Hz	$\tilde{\gamma}, \tilde{\gamma}$	400, -300 Hz s^{-1}
\mathbf{Q}_e	$\text{diag}(0.1, 0.1, 0.1)$	$\mathbf{Q}_v, \mathbf{Q}_{a N}$	$\text{diag}(10, 10), \text{diag}(0.1, 0.1, 0.1)$
$\mathbf{Q}_u, \mathbf{Q}_{v N}$	$\text{diag}(10, 10), \text{diag}(10, \dots, 10)$	P_U, P_J	1W, 1W
σ_J, q_π	$1\sqrt{W}, 1 \times 10^4$	τ_{E_s} , on-off	2s, 5s

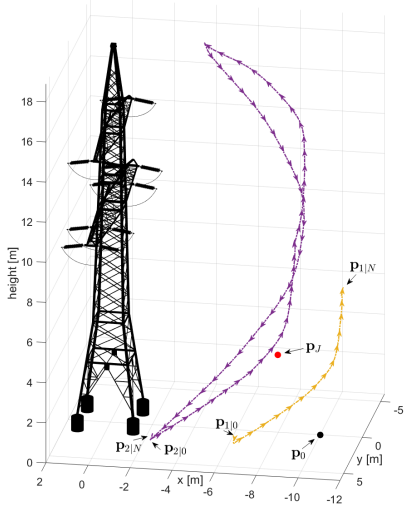


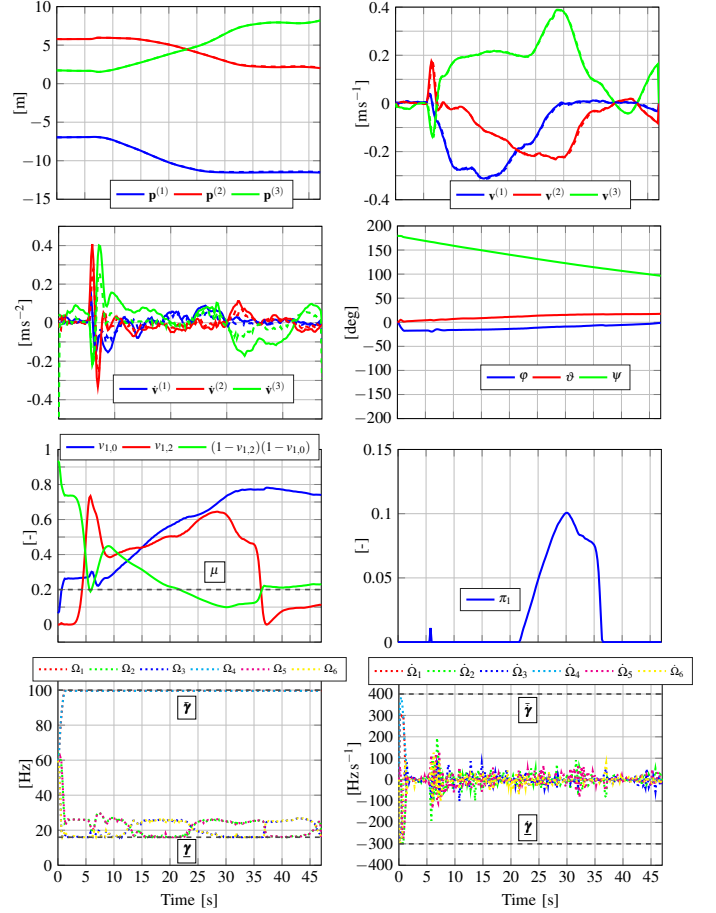
Figure 5: Simulation overview showing the relay (MRAV-1, yellow), the source (MRAV-2, purple), the ground BS (black dot), and the jammer (red dot). Arrows indicate the motion direction.

transmitting with constant radiated power. The jammer acts as an isotropic source and is assumed to be localized after $\tau_E = 2$ s. The simulated workspace spans $14\text{m} \times 12\text{m} \times 19\text{m}$.

The simulations consider a tilted-propeller platform with six rotors, enabling independent control of translation and rotation for accurate antenna alignment under dynamic constraints. System and control parameters, reported in Table II, are chosen to be representative of medium-scale MRAV used in experimental research. The prediction horizon is $T = 0.45$ s, discretized into $N = 30$ shooting nodes. Control inputs are rotor acceleration commands $\hat{\boldsymbol{\Omega}}$, updated at 500Hz and applied to the MRAV-1's model (see Section V-A) integrated at 1kHz to capture fast actuation dynamics.

The proposed NMPC optimizes the motion of MRAV-1 by jointly minimizing trajectory tracking error (21), antenna misalignment (23), and actuator rate variation (22) (see Section VI-B). Figure 5 shows a representative simulation outcome, with MRAV-1 and MRAV-2 trajectories, the BS, and the jammer. Arrows indicate the motion from the initial ($\mathbf{p}_{\bullet|0}$) to final ($\mathbf{p}_{\bullet|N}$) positions.

Figure 6 presents the evolution of key state and control variables subject to constraints in the NMPC formulation. Rotor angular velocities $\boldsymbol{\Omega}$ and their rates $\dot{\boldsymbol{\Omega}}$ remain within the prescribed limits ($\tilde{\gamma}, \tilde{\gamma}, \dot{\tilde{\gamma}}, \dot{\tilde{\gamma}}$), confirming compliance with actuation bounds. A short activation of the slack variable π corresponds to a minor relaxation of the mutual alignment con-


 Figure 6: Time evolution of constrained variables in the NMPC problem. Solid lines: references; dashed: measured values. Superscripts $\bullet^{(1)}$, $\bullet^{(2)}$, and $\bullet^{(3)}$ denote x -, y -, and z -axis components, respectively.

straint (27f), preserving feasibility under transient geometric configurations. The mutual misalignment metric stays above the threshold μ for most of the mission, indicating that the channel degradation due to antenna misalignment is contained despite aggressive maneuvers. Overall, the results confirm that the controller enforces tracking, alignment, and actuation objectives simultaneously while preserving constraint feasibility through penalized soft constraints.

Figure 7 shows the time evolution of the tracking errors in position, velocity, and thrust direction, together with the misalignment penalties (23). The velocity \mathbf{e}_v and thrust-direction \mathbf{e}_p errors remain bounded and converge rapidly after short transients, confirming accurate dynamic regulation. The misalignment penalties $e_{\text{mis}}^{(1)}$ and $e_{\text{mis}}^{(2)}$ remain below 0.6 for most of the mission, with brief peaks during fast reorientations, indicating that the communication links are consistently preserved within acceptable alignment margins. This behavior illustrates the controller's ability to balance positional precision with sustained communication quality and constraint satisfaction.

Figure 8 shows the instantaneous spectral efficiencies $\log_2(1 + \Gamma_{1,0})$ and $\log_2(1 + \Gamma_{2,1})$, together with the resulting

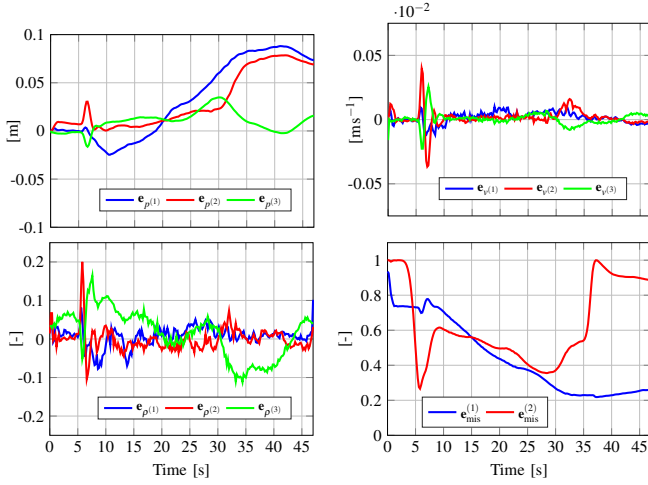


Figure 7: Time evolution of tracking errors in position, velocity, and thrust direction, along with the antenna misalignment penalty components.

end-to-end channel capacity (7), for both the *constrained* and *unconstrained* formulations. In the unconstrained case, antenna-alignment penalties (23) and constraints (27f) are removed from the optimization (27); in the constrained case, they are enforced. The main impact of the constrained formulation is on reliability rather than on mean throughput: the minimum instantaneous end-to-end capacity increases from 7.29×10^{-5} (unconstrained, $C^{(\text{unconstr.})}$) to 6.8×10^{-3} (constrained, $C^{(\text{constr.})}$), i.e., almost two orders of magnitude. This converts near-outage events into usable operating points.

Average gains are more moderate: over the mission, $C^{(\text{constr.})}$ exceeds $C^{(\text{unconstr.})}$ by 1.7%, while $\log_2(1 + \Gamma_{1,0})$ and $\log_2(1 + \Gamma_{2,1})$ increase by 16.9% and 5%, respectively. This behavior is expected because the optimization targets end-to-end robustness, which is bottleneck-limited by the weaker link, rather than monotonic improvement of each link at every instant. As a result, local trade-offs between links may occur, but deep fades are strongly suppressed and outage probability is reduced, which is the key requirement for real-time inspection data streaming. These benefits are expected to become more pronounced with more directive antennas. The approach remains antenna-model agnostic because it relies on geometric alignment metrics rather than explicit radiation-pattern parameterization.

A. Coplanar and tilted-propeller MRAV configurations

This section examines how MRAV mechanical designs, specifically coplanar versus tilted-propeller designs, affects the controller's ability to maintain directional communication. The goal is to isolate how actuation geometry influences the preservation of antenna alignment during motion under interference.

In the coplanar case, all propeller lie on a single plane and generate thrust only along the body z_B -axis, so any lateral motion requires platform tilting, inherently coupling translation with antenna orientation. The tilted-propeller configuration provides partial decoupling between translation and rotation,

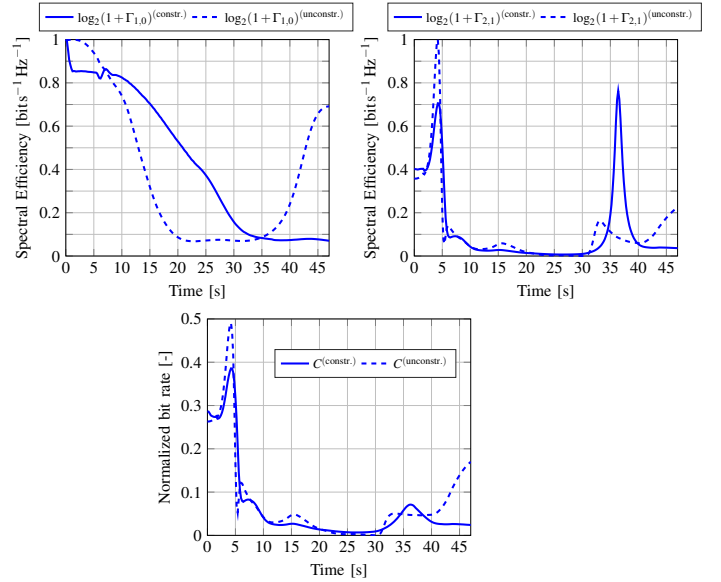


Figure 8: Instantaneous spectral efficiencies $\log_2(1 + \Gamma_{1,0})$ and $\log_2(1 + \Gamma_{2,1})$ and instantaneous end-to-end channel capacity (7). Constrained and unconstrained formulations are compared to isolate the effect of antenna-alignment penalties on relay-BS and source-relay communication performance.

enabling direct lateral thrust with minima attitude changes and thus more favorable conditions for maintaining alignment.

To enable a direct comparison, both vehicles are modeled using the GTMR framework [15], [41], which provides a unified dynamic representation. This ensures that the NMPC structure remains identical across platforms, while differences in feasible wrench sets capture the influence of mechanical actuation alone.

Figure 9 compares constrained (Figures 9a–9c) and unconstrained (Figures 9b–9d) scenarios. In the unconstrained cases, where antenna misalignment penalties are omitted from the optimization problem, the relay exhibits large attitude excursions and wide lateral deviations. The resulting trajectories are longer and more less direct paths, driven purely by geometric tracking without accounting for directional gain degradation. When alignment constraints are enforced, the relay actively regulates its position and orientation to preserve dual link alignment, yielding smoother and more compact paths that remain close to the communication axis connecting the source and base station. This confirms that explicit alignment awareness markedly improves communication-efficient motion.

The alignment-constrained trajectories reveal the clearest differences between the two platforms. In the coplanar configuration (Figure 9a), lateral motion requires significant body tilting because thrust is generated only along the z_B direction. This strongly couples translation and antenna pointing, reduces simultaneous alignment with both peers, and drives the vehicle toward actuation limits. To maintain acceptable alignment, the NMPC increases altitude-up to about 16m, where the LoS geometry enlarges the feasible intersection of the two alignment cones. By contrast, the tilted-propeller configuration (Figure 9b) can generate lateral forces with minimal attitude

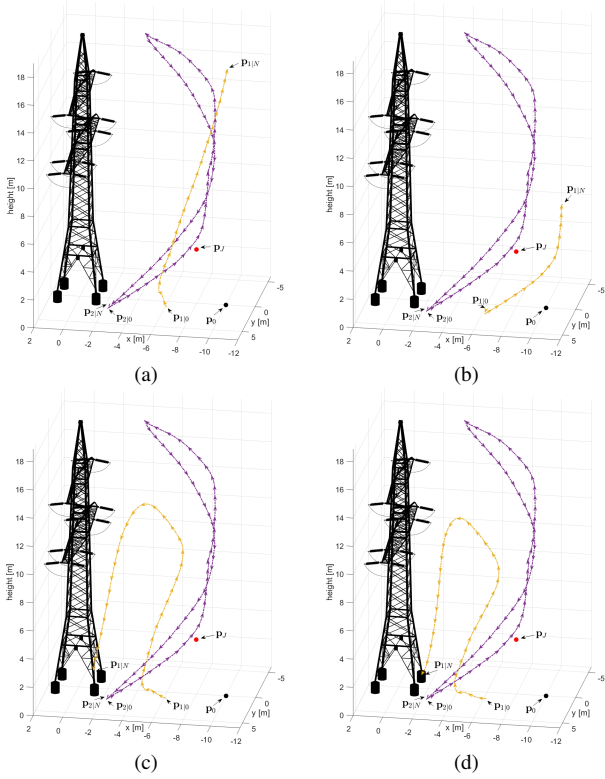


Figure 9: Simulation overviews for coplanar (9a-9c) and tilted-propeller (9b-9d) MRV configurations, shown with (9a-9b) and without (9c-9d) antenna misalignment cost and constraints.

changes. This partial decoupling preserves beam orientation during maneuvers, allowing the relay to follow a shorter, lower trajectory (ending near 8 m) while fully satisfying alignment and actuation constraints.

Figure 10 further shows that actuation geometry strongly affects the communication gains achievable by the constrained formulation. End-to-end performance improves in both platforms, but the improvement is larger for the tilted-propeller design: the average end-to-end capacity increases by 1.7% for the tilted platform and by 0.55% for the coplanar platform. This gap is consistent with the vehicle mechanics. In coplanar vehicles, lateral motion requires roll and pitch, which directly perturb antenna pointing toward the ground BS and make simultaneous optimization of both links more difficult. Hence, stronger local trade-offs between links are unavoidable. In tilted-propeller vehicles, lateral force can be generated with smaller attitude excursions, preserving antenna alignment more effectively during maneuvering. Quantitatively, the constrained formulation improves relay-BS and source-relay spectral efficiencies by 16.9% and 5% in the tilted case, compared with 12.49% and 2.41% in the coplanar case. This trend is consistent with fewer slack-variable activations and fewer near-active alignment constraints, indicating larger feasibility margins and tighter alignment control.

Overall, both platforms remain dynamically feasible under interference, but their communication performance differs sub-

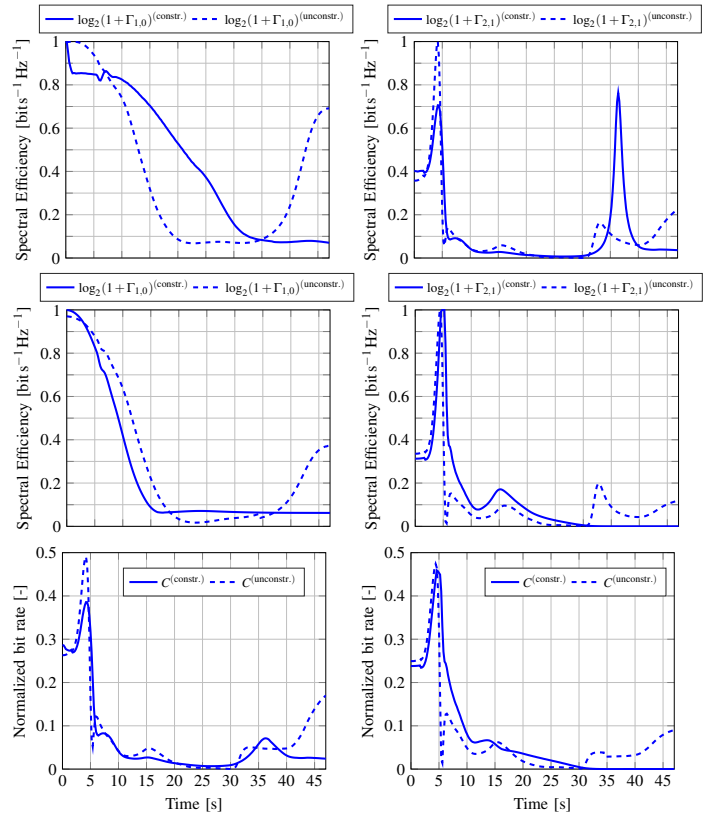


Figure 10: Instantaneous spectral efficiencies and instantaneous end-to-end capacity for both the constrained and unconstrained formulations. The top row corresponds to the tilted-propeller platform, the middle row to the coplanar design. The bottom row compares the end-to-end capacities side-by-side for the tilted-propeller (left) and coplanar (right) designs.

stantially. In the coplanar configuration, translation-attitude coupling causes progressive misalignment and a collapse of end-to-end capacity after approximately 30s. By contrast, the tilted-propeller platform preserves antenna alignment throughout the mission, avoiding outages and maintaining non-zero throughput under persistent jamming. These results indicate that actuation geometry is a determining factor for communication reliability: full actuation (via tilted propellers or equivalent mechanisms) enables robust anti-jamming operation, while standard coplanar designs are mechanically ill-suited for sustained directional communication under interference.

B. Robustness under time-varying jamming

This section assesses the robustness of the proposed communications-aware NMPC when interference is not persistent but time-varying. To emulate more realistic adversarial behavior, the jammer alternates between active and inactive phases, following a periodic ON-OFF schedule (5 s active, 5 s inactive). In the model, the jammer “OFF” phase is implemented by setting its transmit power to zero (i.e., $P_J = 0$), so the jamming term is fully removed from the channel equations during those intervals. This timescale is significantly longer than the vehicle dynamics, allowing a meaningful evaluation of

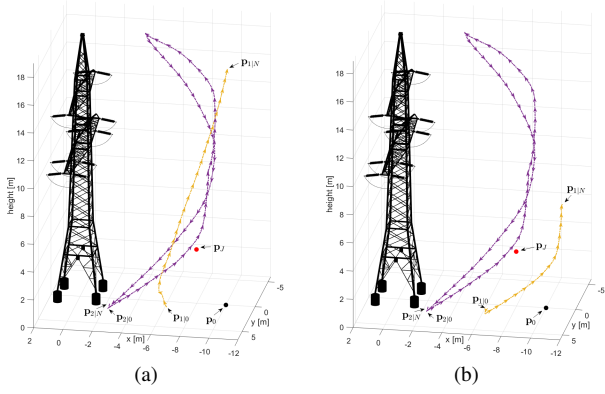


Figure 11: Simulation overviews for coplanar (11a) and tilted-propeller (11b) MRAV configurations under an ON–OFF jamming pattern.

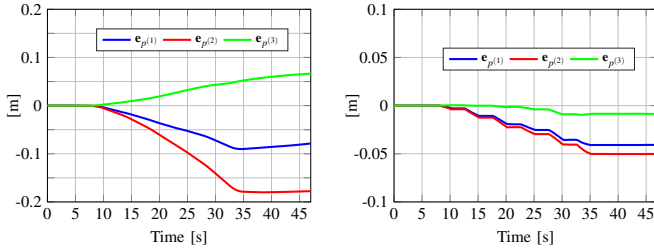


Figure 12: Trajectory deviation between the always-ON and ON–OFF jamming scenarios for coplanar (left) and tilted-propeller (right) MRAV configurations.

the controller’s ability to handle abrupt changes in interference while preserving directional communication.

When the jammer is active, both communication links experience a capacity drop due to intentional RF degradation. Unlike the always-ON scenario, however, the intermittent nature of interference reveals how rapidly the system can recover performance once the disturbance subsides. Importantly, the 3D trajectories (Figure 11) obtained under ON–OFF jamming closely match those from the always-active case: the controller maintains nearly the same relative geometry, altitude, and attitude evolution throughout the entire horizon. This indicates that the NMPC does not overly react to temporary improvements in channel conditions but instead chooses a stable and alignment-optimal configuration that remains effective across interference transitions.

Figure 12 quantifies the difference between the always-ON and ON–OFF trajectories. The deviation remains small over the entire simulation, ranging approximately within $[-0.2, 0.2]$ m for the coplanar platform and $[-0.05, 0.05]$ m for the tilted-propeller one. These values are consistent with the controller’s horizon and update rate: because the ON–OFF cycle (10 s) is significantly longer than the system’s dynamic response time, the optimizer converges to a steady, alignment-preserving motion that remains near-invariant across jamming transitions. The reduced deviation for the tilted-propeller case further reflects its enhanced actuation redundancy, which enables tighter tracking and less sensitivity to transient changes in interference conditions.

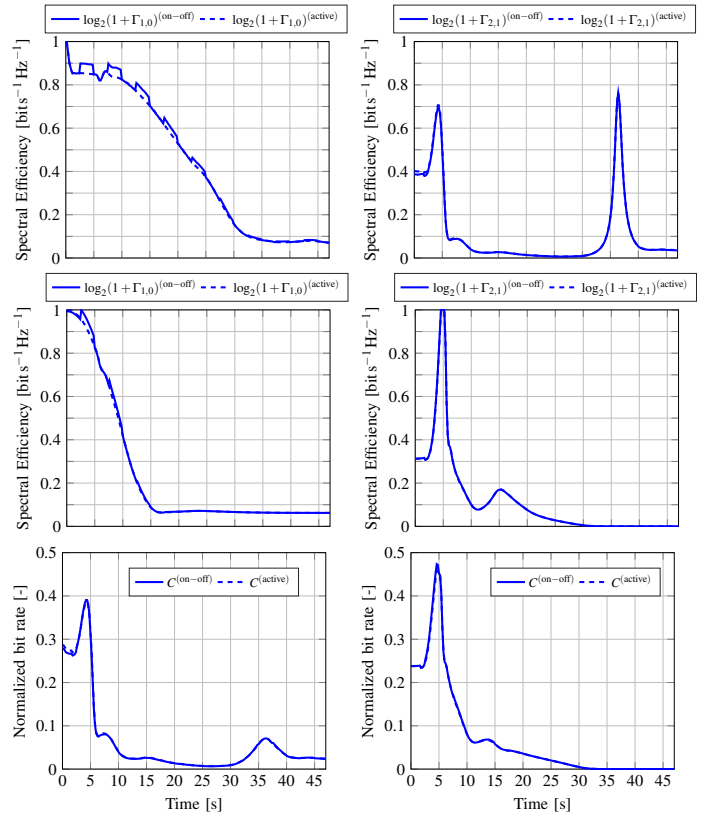


Figure 13: Instantaneous spectral efficiencies under ON–OFF jamming for the tilted-propeller (top) and coplanar (middle) configurations. The bottom row compares the instantaneous end-to-end channel capacities side-by-side for the tilted-propeller (left) and coplanar (right) designs.

As illustrated in Figure 13, the communication results provide a clearer signature of robustness. The instantaneous spectral efficiency $\log_2(1 + \Gamma_{2,1})$ remains largely unaffected by the alternating jammer due to its favorable geometry. In contrast, the spectral efficiency $\log_2(1 + \Gamma_{1,0})$ exhibits a characteristic square-wave modulation: during jammer-ON intervals the capacity drops to the same level observed in the always-active case, but it immediately returns to the high-alignment regime as soon as the jammer turns OFF. Importantly, the difference between the ON–OFF and always-ON capacities (bottom row) is negligible over the full horizon: the controller already adopts a geometry that is optimal for the worst-case (jammer-ON) condition, so capacity recovers automatically to the same high-alignment regime as soon as jamming ceases. In other words, the ON–OFF pattern does not introduce additional outages; it simply toggles the link between its worst-case and best-case operating points.

Overall, the ON–OFF jamming scenario highlights that the proposed NMPC maintains actuation feasibility, alignment quality, and communication robustness even under time-varying interference. The controller does not chase transient fluctuations but instead sustains a geometry that guarantees fast, automatic restoration of link quality when interference ceases.

VIII. CONCLUSIONS

This paper presented a modular communications-aware control framework that integrates a max–min trajectory generator with a Nonlinear Model Predictive Controller for MRAVs operating under jamming. The framework jointly considers vehicle dynamics, actuator limits, and directional antenna constraints, enabling MRAVs to sustain end-to-end RF connectivity while executing dynamically feasible maneuvers.

Simulations show that enforcing antenna-alignment constraints enhances communication robustness by mitigating deep capacity drops and stabilizing throughput. The magnitude of these benefits, however, depends strongly on actuation geometry. The tilted-propeller platform maintains consistently higher link quality, whereas the coplanar vehicle exhibits reduced performance and even experiences a temporary loss of connectivity in the final portion of the mission. Under ON–OFF jamming, the controller preserves alignment during active interference and restores throughput immediately when the jammer turns OFF, confirming resilience to intermittent degradation. Overall, embedding communication objectives into the control loop improves robustness, with platform-dependent gains.

Future work will focus on two main directions. First, integrating online estimation of jammer characteristics and adaptive adjustment of alignment constraints to enhance resilience against rapidly varying interference. Second, validating the framework on real coplanar and tilted-propeller MRAV platforms to assess the impact of unmodeled dynamics such as aerodynamic coupling, actuator delays, and sensor latency.

APPENDIX A ANTENNA MODEL

Each node in the MRAV network is equipped with a half-wave dipole antenna rigidly mounted along the body-frame z_{B_j} -axis, consistent with the communication model introduced in Section V-B. The resulting radiation pattern is *doughnut-shaped*, with maximum gain in directions orthogonal to the antenna axis and nulls along the boresight. The antenna of MRAV- j is located at the origin of its body frame O_{B_j} , while the ground BS antenna is placed at the top of the station structure.

The directional gain of each antenna is described by the function $G(\vartheta)$, where $\vartheta \in [0, \pi]$ is the elevation angle between the incident (or departing) signal direction and the antenna axis. For a dipole-type pattern, the gain satisfies $G(0) = G(\pi) = 0$, $G(\pi/2) = \bar{G}$, and is assumed to be azimuthally symmetric, i.e., independent of the angle $\varphi \in [0, 2\pi)$. This definition is consistent with the use of $G(\cdot)$ in the channel and jamming gains (4)–(5).

We now specify how elevation angles are computed for a link between transmitter node i and receiver node j . The Angle of Departure elevation angle measured at node i is

$$\vartheta_i^D = \frac{\pi}{2} - \arctan \left(\frac{\mathbf{a}_j^{(3)}}{\sqrt{\mathbf{a}_j^{(1)2} + \mathbf{a}_j^{(2)2}}} \right), \text{ with } \mathbf{a}_j = \mathbf{R}_j^\top \frac{\mathbf{p}_j - \mathbf{p}_i}{\|\mathbf{p}_j - \mathbf{p}_i\|}. \quad (28)$$

Here, \mathbf{R}_i^\top is the rotation from the world frame \mathcal{F}_W to \mathcal{F}_{B_i} , and \mathbf{a}_j is the unit direction vector from transmitter i to receiver j , expressed in \mathcal{F}_{B_i} . Similarly, the AoA elevation angle at node j is

$$\vartheta_j^A = \frac{\pi}{2} - \arctan \left(\frac{\mathbf{b}_i^{(3)}}{\sqrt{\mathbf{b}_i^{(1)2} + \mathbf{b}_i^{(2)2}}} \right), \text{ with } \mathbf{b}_i = \mathbf{R}_j^\top \frac{\mathbf{p}_i - \mathbf{p}_j}{\|\mathbf{p}_i - \mathbf{p}_j\|}, \quad (29)$$

where \mathbf{R}_j^\top maps vectors from \mathcal{F}_W to \mathcal{F}_{B_j} and \mathbf{b}_i denotes the unit direction from node j to node i expressed in \mathcal{F}_{B_j} .

This formulation explicitly couples antenna orientation to the vehicle attitude and ensures consistency with the gain-based channel model in (4)–(5). The approach is compatible with any doughnut-shaped radiation pattern; representative models for aerial communication applications are available in [17], [35], [47].

APPENDIX B TAYLOR EXPANSION

The Taylor expansion is performed w.r.t both time-varying position vectors \mathbf{p}_1 and \mathbf{p}_2 , which are compactly represented in the composite variable $\boldsymbol{\kappa} \triangleq [\mathbf{p}_1^\top, \mathbf{p}_2^\top]^\top$. This formulation allows the effect of variations in \mathbf{p}_2 to be incorporated explicitly, avoiding the need to re-derive the approximation at each time step.

Let $f(\boldsymbol{\kappa}, P_j)$ denote the cost function (dependent on jammer power P_j), and define its gradient and Hessian as

$$\mathbf{g}(\boldsymbol{\kappa}, P_j) \triangleq \nabla_{\boldsymbol{\kappa}} f(\boldsymbol{\kappa}, P_j), \quad \mathbf{H}(\boldsymbol{\kappa}, P_j) \triangleq \nabla_{\boldsymbol{\kappa}}^2 f(\boldsymbol{\kappa}, P_j). \quad (30)$$

We partition the gradient (expressed as a column vector) into components associated with \mathbf{p}_1 and \mathbf{p}_2 as:

$$\mathbf{g}(\boldsymbol{\kappa}, P_j) = \begin{bmatrix} \mathbf{g}_1(\boldsymbol{\kappa}, P_j) \\ \mathbf{g}_2(\boldsymbol{\kappa}, P_j) \end{bmatrix}, \quad (31)$$

where $\mathbf{g}_1(\boldsymbol{\kappa}, P_j) \triangleq \nabla_{\mathbf{p}_1} f(\boldsymbol{\kappa}, P_j)$ and $\mathbf{g}_2(\boldsymbol{\kappa}, P_j) \triangleq \nabla_{\mathbf{p}_2} f(\boldsymbol{\kappa}, P_j)$.

Similarly, the Hessian is partitioned as:

$$\mathbf{H}(\boldsymbol{\kappa}, P_j) = \begin{bmatrix} \mathbf{H}_{11}(\boldsymbol{\kappa}, P_j) & \mathbf{H}_{12}(\boldsymbol{\kappa}, P_j) \\ \mathbf{H}_{21}(\boldsymbol{\kappa}, P_j) & \mathbf{H}_{22}(\boldsymbol{\kappa}, P_j) \end{bmatrix}, \quad (32)$$

where $\mathbf{H}_{ij}(\boldsymbol{\kappa}, P_j) \triangleq \nabla_{\mathbf{p}_i} \nabla_{\mathbf{p}_j}^\top f(\boldsymbol{\kappa}, P_j)$ for $i, j \in \{1, 2\}$.

The second-order Taylor expansion of $f(\boldsymbol{\kappa}, P_j)$ around the point $\boldsymbol{\kappa}_e = [\mathbf{p}_{1_e}^\top, \mathbf{p}_{2_e}^\top]^\top$ (that we express as $f^{[2]}(\boldsymbol{\kappa}; \boldsymbol{\kappa}_e, P_j)$) reads:

$$\begin{aligned} f^{[2]}(\boldsymbol{\kappa}; \boldsymbol{\kappa}_e, P_j) &= f(\boldsymbol{\kappa}_e, P_j) + \mathbf{g}_1^\top(\boldsymbol{\kappa}_e, P_j) \boldsymbol{\delta}_1 + \\ &\quad \mathbf{g}_2^\top(\boldsymbol{\kappa}_e, P_j) \boldsymbol{\delta}_2 + \frac{1}{2} \boldsymbol{\delta}_1^\top \mathbf{H}_{11}(\boldsymbol{\kappa}_e, P_j) \boldsymbol{\delta}_1 + \\ &\quad + \boldsymbol{\delta}_1^\top \mathbf{H}_{12}(\boldsymbol{\kappa}_e, P_j) \boldsymbol{\delta}_2 + \\ &\quad + \frac{1}{2} \boldsymbol{\delta}_2^\top \mathbf{H}_{22}(\boldsymbol{\kappa}_e, P_j) \boldsymbol{\delta}_2, \end{aligned} \quad (33)$$

where $\boldsymbol{\delta}_1 \triangleq \mathbf{p}_1 - \mathbf{p}_{1_e}$ and $\boldsymbol{\delta}_2 \triangleq \mathbf{p}_2 - \mathbf{p}_{2_e}$.

This formulation enables the MRAV-1 trajectory generator to incorporate variations in the state of MRAV-2 without re-evaluating the full cost function or recomputing the gradient and Hessian at each iteration, thereby reducing computational overhead.

REFERENCES

- [1] A. Muralidharan *et al.*, “Communication-Aware Robotics: Exploiting Motion for Communication,” *Ann. Rev. of Contr., Rob., and Aut. Syst.*, vol. 4, pp. 115–139, 2021.
- [2] Y. Zeng *et al.*, “Accessing From the Sky: A Tutorial on UAV Communications for 5G and Beyond,” *Proc. of the IEEE*, vol. 107, no. 12, pp. 2327–2375, 2019.
- [3] D. Bonilla Licea *et al.*, “When Robotics Meets Wireless Communications: An Introductory Tutorial,” *Proc. of the IEEE*, vol. 112, no. 2, pp. 140–177, 2024.
- [4] W. Hurst *et al.*, “Uncrewed Vehicles in 6G Networks: A Unifying Treatment of Problems, Formulations, and Tools,” *Proc. of the IEEE*, pp. 1–35, 2025, In Press.
- [5] M. Mozaffari *et al.*, “A Tutorial on UAVs for Wireless Networks: Applications, Challenges, and Open Problems,” *IEEE Comm. Surv. Tut.*, vol. 21, no. 3, pp. 2334–2360, 2019.
- [6] Y. Zeng *et al.*, “Cellular-Connected UAV: Potential, Challenges, and Promising Technologies,” *IEEE Wirel. Comm.*, vol. 26, no. 1, pp. 120–127, 2019.
- [7] R. Shakeri *et al.*, “Design Challenges of Multi-UAV Systems in Cyber-Physical Applications: A Comprehensive Survey and Future Directions,” *IEEE Comm. Surv. Tut.*, vol. 21, no. 4, pp. 3340–3385, 2019.
- [8] M. Stachura *et al.*, “Communication-Aware Information-Gathering Experiments with an Unmanned Aircraft System,” *J. of Fie. Rob.*, vol. 34, no. 4, pp. 736–756, 2017.
- [9] C. Zhong *et al.*, “Secure UAV Communication With Cooperative Jamming and Trajectory Control,” *IEEE Comm. Lett.*, vol. 23, no. 2, pp. 286–289, 2019.
- [10] Z. Ji *et al.*, “Trajectory and Transmit Power Optimization for IRS-Assisted UAV Communication Under Malicious Jamming,” *IEEE Trans. Veh. Technol.*, vol. 71, no. 10, pp. 11 262–11 266, 2022.
- [11] G. Silano *et al.*, “Free-Space Optical Communication-Driven NMPC Framework for Multi-Rotor Aerial Vehicles in Structured Inspection Scenarios,” in *IEEE Int. Conf. on Syst., Man and Cyber.*, 2025, pp. 6649–6654.
- [12] D. Bonilla Licea *et al.*, “Omnidirectional Multi-Rotor Aerial Vehicle Pose Optimization: A Novel Approach to Physical Layer Security,” in *IEEE Int. Conf. on Aco., Spe. and Sig. Proc.*, 2024, pp. 9021–9025.
- [13] S. Vadlamani *et al.*, “Jamming attacks on wireless networks: A taxonomic survey,” *Int. J. Prod. Econ.*, vol. 172, pp. 76–94, 2016.
- [14] P. Ribeiro *et al.*, “On the Energy Consumption of Rotary-Wing and Fixed-Wing UAVs in Flying Networks,” in *Wirel. On-Dem. Netw. Syst. Serv.*, 2025, pp. 1–4.
- [15] M. Ryll *et al.*, “6D interaction control with aerial robots: The flying end-effector paradigm,” *Int. J. Rob. Res.*, vol. 38, no. 9, pp. 1045–1062, 2019.
- [16] D. Bonilla Licea *et al.*, “Reshaping UAV-Enabled Communications with Omnidirectional Multi-Rotor Aerial Vehicles,” *IEEE Com. Mag.*, vol. 63, no. 5, pp. 94–100, 2025.
- [17] J. Chen *et al.*, “Impact of 3D UWB Antenna Radiation Pattern on Air-to-Ground Drone Connectivity,” in *IEEE Veh. Tech. Conf.*, 2018, pp. 1–5.
- [18] P. Lohan *et al.*, “From 5G to 6G Networks: A Survey on AI-Based Jamming and Interference Detection and Mitigation,” *IEEE Open J. Commun. Soc.*, vol. 5, pp. 3920–3974, 2024.
- [19] S. Zhang *et al.*, “Cellular-Enabled UAV Communication: A Connectivity-Constrained Trajectory Optimization Perspective,” *IEEE Trans. Commun.*, vol. 67, no. 3, pp. 2580–2604, 2019.
- [20] E. Bulut *et al.*, “Trajectory Optimization for Cellular-Connected UAVs with Disconnectivity Constraint,” in *IEEE Int. Conf. on Comm.*, 2018, pp. 1–6.
- [21] B. Khamidehi *et al.*, “A Double Q-Learning Approach for Navigation of Aerial Vehicles with Connectivity Constraint,” in *IEEE Int. Conf. on Comm.*, 2020, pp. 1–6.
- [22] Y. Zeng *et al.*, “Simultaneous Navigation and Radio Mapping for Cellular-Connected UAV With Deep Reinforcement Learning,” *IEEE Trans. Wirel. Comm.*, vol. 20, no. 7, pp. 4205–4220, 2021.
- [23] U. Challita *et al.*, “Interference Management for Cellular-Connected UAVs: A Deep Reinforcement Learning Approach,” *IEEE Trans. Wirel. Comm.*, vol. 18, no. 4, pp. 2125–2140, 2019.
- [24] Y. Xu *et al.*, “Joint Power and Trajectory Optimization in UAV Anti-Jamming Communication Networks,” in *IEEE Int. Conf. on Comm.*, 2019, pp. 1–5.
- [25] B. Duo *et al.*, “Anti-Jamming 3D Trajectory Design for UAV-Enabled Wireless Sensor Networks Under Probabilistic LoS Channel,” *IEEE Trans. Veh. Technol.*, vol. 69, no. 12, pp. 16 288–16 293, 2020.
- [26] Y. Wu *et al.*, “UAV-UAV Communication Under Malicious Jamming: Trajectory Optimization with Turning Angle Constraint,” in *Int. Conf. Wirel. Comm. Sig. Proc.*, 2020, pp. 26–31.
- [27] W. Xu *et al.*, “Channel surfing and spatial retreats: defenses against wireless denial of service,” in *ACM Worksh. Wirel. Sec.*, 2004, pp. 80–89.
- [28] Y. Li *et al.*, “Cooperative Jamming for Secure UAV Communications With Partial Eavesdropper Information,” *IEEE Acc.*, vol. 7, pp. 94 593–94 603, 2019.
- [29] S. Bhattacharya *et al.*, “Game-theoretic analysis of an aerial jamming attack on a UAV communication network,” in *Ame. Contr. Conf.*, 2010, pp. 818–823.
- [30] K. Judd *et al.*, “Spline based path planning for unmanned air vehicles,” in *AIAA Guid., Nav., Control Conf.*, 2001, pp. 4238–4246.
- [31] Y. Duan *et al.*, “Route planning method design for UAV under radar ECM scenario,” in *Int. Conf. Sig. Proc.*, 2014, pp. 108–114.
- [32] S. Lv *et al.*, “Anti-Jamming Power Control Game in Unmanned Aerial Vehicle Networks,” in *IEEE Glob. Commun. Conf.*, 2017, pp. 1–6.
- [33] X. Wenyuan *et al.*, “Jamming sensor networks: attack and defense strategies,” *IEEE Netw.*, vol. 20, no. 3, pp. 41–47, 2006.
- [34] X. Lu *et al.*, “UAV-Aided Cellular Communications with Deep Reinforcement Learning Against Jamming,” *IEEE Wirel. Comm.*, vol. 27, no. 4, pp. 48–53, 2020.
- [35] D. Bonilla Licea *et al.*, “Optimum Trajectory Planning for Multi-Rotor UAV Relays with Tilt and Antenna Orientation Variations,” in *Eur. Sig. Proc. Conf.*, 2021, pp. 1586–1590.
- [36] M. Z. Chowdhury *et al.*, “Optical Wireless Hybrid Networks: Trends, Opportunities, Challenges, and Research Directions,” *IEEE Comm. Surv. Tut.*, vol. 22, no. 2, pp. 930–966, 2020.
- [37] J. Horyna *et al.*, “UVDAR-COM: UV-Based Relative Localization of UAVs with Integrated Optical Communication,” in *Int. Conf. on Unm. Air. Sys.*, 2022, pp. 1302–1308.
- [38] D. Bonilla Licea *et al.*, “Optical communication-based identification for multi-UAV systems: theory and practice,” *Aut. Rob.*, vol. 49, no. 4, pp. 1–17, 2025.
- [39] S. Bhamidipati *et al.*, “Locating Multiple GPS Jammers Using Networked UAVs,” *IEEE Int. Thin. J.*, vol. 6, no. 2, pp. 1816–1828, 2019.
- [40] M. Juhlin *et al.*, “Localization Of Multiple Jammers in Wireless Sensor Networks,” in *Eur. Sig. Proc. Conf.*, 2021, pp. 1596–1600.
- [41] M. Hamandi *et al.*, “Design of multirotor aerial vehicles: A taxonomy based on input allocation,” *Int. J. Rob. Res.*, vol. 40, no. 8-9, pp. 1015–1044, 2021.
- [42] J. Laneman *et al.*, “Cooperative diversity in wireless networks: Efficient protocols and outage behavior,” *IEEE Trans. Inf. Theory*, vol. 50, no. 12, pp. 3062–3080, 2004.
- [43] A. Goldsmith, *Wireless Communications*. Cambridge University Press, 2005.
- [44] Y. Chen *et al.*, “MATMPC - A MATLAB Based Toolbox for Real-time Nonlinear Model Predictive Control,” in *Eur. Contr. Conf.*, 2019, pp. 3365–3370.
- [45] H. Ferreau *et al.*, “qpOASES: A parametric active-set algorithm for quadratic programming,” *Math. Progr. Comp.*, vol. 6, no. 4, pp. 327–363, 2014.
- [46] G. Silano *et al.*, “Power Line Inspection Tasks With Multi-Aerial Robot Systems Via Signal Temporal Logic Specifications,” *IEEE Robot. Autom. Lett.*, vol. 6, no. 2, pp. 4169–4176, 2021.
- [47] E. Turgut *et al.*, “Energy Harvesting in Unmanned Aerial Vehicle Networks With 3D Antenna Radiation Patterns,” *IEEE Trans. Green Commun. Netw.*, vol. 4, no. 4, pp. 1149–1164, 2020.